Tatar-Mathes, Philipp, Hansen, Rasmus E., Choi, Samuel, Marques, M.J., Israelsen, Niels Møller and Podoleanu, Adrian G.H. (2024) *Temperature Dependence of a Depth-Encoded System for Polarization-Sensitive Optical Coherence Tomography using a PM Fiber.* In: Proceedings Volume 13187, Advances in 3OM: Opto-Mechatronics, Opto-Mechanics, and Optical Metrology (3OM 2023). 13187 (2024). SPIE, Romania

Temperature Dependence of a Depth-Encoded System for Polarization-Sensitive Optical Coherence Tomography using a PM Fiber

PHILIPP TATAR-MATHES,[1,†,*] RASMUS EILKÆR HANSEN,[2,†] SAMUEL CHOI [3,†], MANUEL J. MARQUES,[4] NIELS MØLLER ISRAELSEN, [2] AND ADRIAN PODOLEANU [4]

[†] *The authors contributed equally to this work.*

[1]*Optoelectronics Research Center, Physics Unit/ Photonics, Tampere University, Korkeakoulunkatu 3, 33720 Tampere, Finland*

[2]*DTU Electro, Department of Electrical and Photonics Engineering, Technical University of Denmark, 2800 Kgs. Lyngby, Denmark*

[3]*Niigata University, Department of Electrical and Electronics Engineering, 8050 Ikarashi-2, Niigata 950-2181, Japan*

[4]*Applied Optics Group, School of Physics and Astronomy, Division of Natural Sciences, University of Kent, Canterbury CT2 7NH, United Kingdom*

[*]*philipp.tatar-mathes@tuni.fi*

Abstract: With the aim of applying complex master/slave interferometry (CMSI) to polarization-sensitive optical coherence tomography (PS-OCT) for birefringent tomographic measurements of biological tissue, we present the impact of temperature instability on an all-fiber-based depth-encoded PS-OCT system and the practicality of temperature control for birefringence measurements. In our PS-OCT system, two orthogonally polarized interrogating beams were separated to a depth of approximately 1 mm using a 5-meter long polarization-maintaining fiber (PMF) as a passive delay unit, which is susceptible to temperature instability. The variation in resolution and delay due to temperature change of PMF were investigated. Furthermore, it is shown that tomographic birefringence can be measured under temperature-controlled operation utilizing the advantages of CMSI. We found that changes to the location of generated masks caused by an emerging temperature drift between the channels can be corrected with our presented characterization.

1. Introduction

Optical coherence tomography (OCT) is a non-destructive imaging technique capable of delivering depth-resolved images of translucent tissue. Since its first report in 1991 [1], OCT has evolved into the *de facto* technology in ophthalmic imaging, and more recently into other medical imaging sub-fields [2]. Since the first polarization-sensitive OCT (PS-OCT) [3] was reported, various types of PS-OCT have been proposed and applied in a wide range of fields. In particular, the visualization of birefringence and collagen alignment enabled by PS-OCT [4, 5] can help assess additional tissue contrast when compared to standard OCT. For instance, the sclera, retinal nerve fiber layer, and corneal stroma display birefringent properties in the eye, hence the application to ophthalmology including anterior and posterior eye imaging [6–14] has been attempted as well as the early applications of OCT. But also apart from the eye, PS-OCT has been applied in many biomedical fields including skin imaging [15–18], dental imaging [19, 20], anterior and posterior eye imaging [6–14], as well as the characterization of atherosclerotic plaque inside blood vessels [21–23]. Recent applications also include the investigation of bronchial airways [24–31], such as pre-clinical studies for retinal disorders. Besides clinical applications, for biologists studying the reproductive capabilities of cells, this information can offer insights into the dynamics by tracking the changes in birefringence over time [32–36]. The functional extension to polarimetry that enables the applications listed above explores one of

the conditions for interference: that of matching the polarization state of the light waves in the two interferometer arms. PS-OCT detects two orthogonal polarization states from the sample separately. This method allows to conclude about the polarization properties of the tissue, i.e., double pass phase retardation (DPPR) and the orientation of the optical axis. The most common implementation of PS-OCT probes the sample with a single, circularly-polarized state [3]. This is often realized using bulk polarization optics and free space propagation, as it is necessary to ensure a stable polarization state over time, which is not possible when using single-mode fibers [37]. To preserve the orientation of polarization, polarization-maintaining fibers (PMF) can be used [38] to provide passive polarization multiplexing. However, PMF-based PS-OCT systems present their own set of challenges, such as polarization-mode dispersion (PMD) and the birefringence properties of the incorporated PMF. In this study, a swept source PS-OCT system based on multiple-input state configuration was constructed as an all-fiber-optic-based system for translation and adaptation to numerous applications, including endoscopy. The system employs passive polarization multiplexing by encoding different polarization states at different depths within a single A-scan [39]. In order to separate the two orthogonal depth-resolved interrogating polarization channels, we use PMF for the passive delay unit in a similar way to that reported by Wang et al. [40], which removes the need for spatial alignment of the system. In addition, the complex master/slave interferometry (CMSI) procedure [41] was applied as a dispersion compensation method to resolve the resolution degradation caused by both the unmatched fiber length between the reference and sample arms and the PMD due to the several meter long PMF. This approach does not require additional components to separate the channels from the PMF, however, it assumes that environmental parameters such as temperature and mechanical stress are stable enough to ensure consistent channel separation. In particular, the temperature-dependent length of the PMF can affect the proper dispersion setting of CMSI and lead to OCT image degradation. Furthermore, changes in the optical path difference (OPD) can impede detection of object surfaces, which will impact in the estimation of the DPPR and orientation. This paper presents the temperature dependence of the PMF used to separate the channels and its impact on the performance of an all-fiber based PS-OCT system with CMSI applied. In particular, we analyze the variation of the axial resolution and the depth distance difference between passively multiplexed channels, and its impact on the dispersion behavior of the setup when varying the temperature.

2. Method

In order to separate the two orthogonal interrogating polarization states, these are multiplexed in two depth-resolved channels in the OCT signal. While this approach does not require any additional components to separate the channels apart from a PMF, it assumes that the environmental parameters (temperature, mechanical stress etc) are stable enough to ensure consistent channel separation. The findings related to the PMF temperature-dependent performance are applied to obtain OCT images of a plastic hair comb with birefringent features, followed by a biological sample. The experimental setup is a fiber-based PS-OCT system that employed the method of Wang et al. [40] and is schematically illustrated in Fig.1. Light from a swept source (Axsun, central wavelength of 1360 nm, tuning range of $\approx$ 100 nm) with a sweep rate of 100 kHz, was split up into a sample and reference arm. In the sample arm, a 5 m long PMF generated two orthogonal polarization modes for the interrogating beam separated from each other by a delay distance determined by PMD. The distance of the delayed polarization channel corresponds to $(n_2 - n_1) \cdot L$, where n_1 and n_2 are the effective refractive indices of orthogonal polarization axes in the PMF for the different polarization modes, and L denotes the length of the PMF. This delay due to the PMD and birefringence properties of the PMF enables the detection of two polarization modes that are multiplexed into different optical path differences. The reference arm was adjusted to have the same optical path as the sample arm by using a single mode (SM) fiber

of the same length as the PMF. The interference signal was divided into vertically polarized (V channel) and horizontally polarized (H channel) beams by a polarization fiber coupler, and each was detected by balanced detector units (PDB435C-AC with 350 MHz bandwidth (800-1700 nm), Thorlabs). These signals are digitized using a high speed digitizer (Alazar ATS9360, 12-bit, 1.8 GS/s). This detection unit consists of two in-fiber polarization controllers which can be used, in conjunction with the fiber-based polarization beam splitters, to ensure the selection of two orthogonal polarization states from the sample arm. The calibration was performed according to the procedure indicated in [40] using a calibration port prior to performing the measurements. Each orthogonal polarization state was separated into non-delayed and delayed signals by the effect of PMD, resulting in a total of four channels (PM1-V, PM2-V, PM1-H, and PM2-H) being detected by the detection unit.
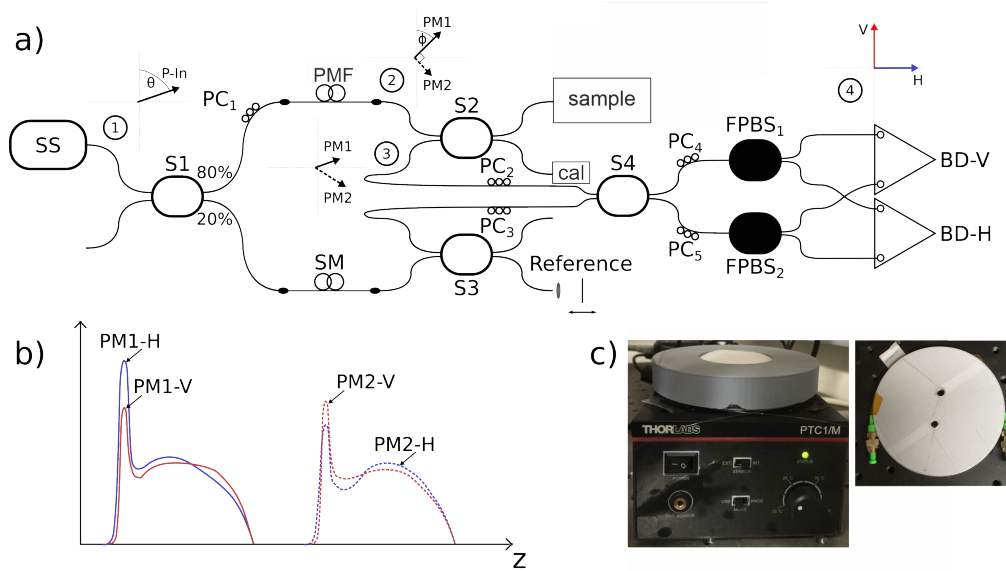

Fig. 1. **a)** A sketch of the PS-OCT setup. Along with the setup, the polarization state of the light is shown in four different positions, numbered accordingly. **SS** swept source, **S1-4** splitter 1-4, **PC1-5** polarization controller 1-5, **PMF** polarization maintaining fiber, **SM** single mode fiber, **cal** calibration port, **FPBS** fiber based polarization beam-splitter, **BD-V,H** Balanced detection in vertical and horizontal channels, **P-In** input polarization state, **PM1,2** polarization states corresponding to fast and slow axes in PMF. **b)** An example of a single A-scan obtained with the setup. The vertical and horizontal channels are visualized in blue and red, accordingly. In both channels the two depth resolved signals are measured, here showed in fully drawn and dashed lines according to **a)**. **c)** As the PMF is temperature sensitive, it has been attached to a 3D-printed spool which is put in thermal contact to a stabilized heating plate (Thorlabs PTC1), such that the temperature of the PMF can be kept constant irrespective of the ambient temperature.

Our system is characterized by the application of CMSI [43] to achieve SS-OCT without the need for dispersion compensation and resampling [42]. In the CMSI, the frequency demodulation operation, which corresponds to the A-scan signal, was computed by a simple matrix calculation that relates the synthesised masks of a calibrated "master"-set of matrices with the raw signal. This way, the A-scan representation of a depth-resolved scattering map is retrieved that directly assigns the interference fringes, including dispersion imbalance and wavenumber nonlinearity. Moreover, the number of data points and range of the A-scan can be changed

arbitrarily. Consequently, this formalism allows for significant reduction in computation time if information from a few depths only is needed, such as in the case of generating a few *en-face* OCT images only [41, 43–45]. This requires a "master stage" that measures the channeled spectra from interference fringes with different OPD values beforehand. In the master stage, replicas of the interferometric signal at arbtitrary depths called "masks" are synthesized by the wavelength-dependent phase gradient "$g(\lambda)$" and the intercept phase "$h(\lambda)$" are obtained to enable the matrix operation (i.e. "slave stage") such as those described above. The processing is carried out for both channels of V and H by calling out the relevant masks in the corresponding depth ranges. Within our experiments, the master/slave operation was performed by applying different masks to the non-delayed (PM1-V and PM1-H) and delayed (PM2-V and PM2-H) signals, each with a different depth range depending on the PMD. To investigate the effect of the aforementioned temperature changes, master/slave operations were processed for different temperature settings of the PMF. The polarization-sensitive detection was achieved using fiber based PS-OCT with CMSI as described above.

The detected four channel signals do not directly provide the birefringence and rotation in the sample, but rather of the entire setup including fiber optics. To eliminate the effect of polarization rotation of the optics and obtain only the internal polarization state of the sample, the detected matrices are multiplied by the inverse of the Jones matrix from the sample surface to the detector. The Jones matrix inside the sample can be obtained as the eigenvalues of the product of these matrices. By this eigendecomposition, the DPPR can be correctly recovered from the argument of the ratio of these two eigenvalues [40, 46, 47]. The Eigen-decomposition of the matrix calculations was applied as shown in [40]. We retrieved the Jones matrices of a sample for every single encodable depth, which ultimately enables the calculation of DPPR and diattenuation. The depth-resolved sample orientation α corresponds to the azimuthal angle of elliptical polarization. A general Jones matrix of the linear birefringence can be described as [48]

$$
\begin{pmatrix} a & b \\ c & d \end{pmatrix} = \begin{pmatrix} cos(\alpha) & -sin(\alpha) \\ sin(\alpha) & cos(\alpha) \end{pmatrix} \cdot \begin{pmatrix} exp(-il/2) & 0 \\ 0 & exp(il/2) \end{pmatrix} \cdot \begin{pmatrix} cos(\alpha) & sin(\alpha) \\ -sin(\alpha) & cos(\alpha) \end{pmatrix} \quad (1)
$$

$$
= \begin{pmatrix} cos(l/2) + icos(2\alpha)sin(l/2) & -isin(l/2)sin(2\alpha) \\ -isin(l/2)sin(2\alpha) & cos(l/2) - icos(2\alpha)sin(l/2) \end{pmatrix}
$$

with l being the DPPR. Using this formalism, the angle of orientation can be calculated as

$$
\alpha = \frac{1}{2} Arg\left[Im(da^* + bc^*) + Im(ab^* + dc^*)\right] \quad (2)
$$

The detector units were calibrated following the procedure described in [40]. Both detectors have two channels to enable equal balanced detection. After the procedure, the sample DPPR can be determined correctly, because the fiber optics from S2 to FPBS1 (also from S3 to FPBS2) becomes a pure wave retarder with horizontal optic axis. This calibration was done by injecting linearly polarized light from the SS laser into the calibration port of Fig.1 and adjusting PC4 and PC5 until the signal intensity received at BD-V is at its maximum and simultaneously at BD-H is at its minimum. The best contrast is achieved when there is the same signal in both channels, which corresponds to coupling at 45 degrees with respect to the primary axes of the PMF. Any mechanical movement of the optical fiber, and changes in the ambient conditions will influence the polarization state, therefore it is worth calibrating at every start up.

We retrieved OCT images with DPPR distribution of a sample by detecting the sample surface. Under the assumption that the surface reflection yields a higher signal than the sample at different axial positions, setting a threshold can be applied to automatically acquire the surface values.

From the viewpoint of continuous birefringent observation of a sample for long periods of time, the surface positioning errors and degradation in CMSI operation due to fluctuations in PMF length or PMD delays caused by temperature changes can be a major problem.

3. Results

In preliminary experiments, we have identified that the major fluctuations are due to the temperature dependence of the PMF parameters. The PMF used in our system is of the Panda type, which means the birefringence is stress induced. Along the direction of the fiber there are two rods embedded in the cladding with a higher thermal expansion coefficient than the surrounding glass. When the ambient temperature increases the induced tension reduces, thus making the PMF less birefringent while increasing its effective length due to heat expansion. This fluctuation may affect not only the fiber length but also the delay due to PMD. Therefore, we experimentally investigated the effect of temperature change on the fiber-based PS-OCT system by controlling the temperature of the PMF with a thermostat as shown in Fig.1 c). The effect of ambient temperature changes in the PMF to the PS-OCT setup is presented in the following section. In our experiments, we ensured that both channels lay within the axial range allowed by the k-clock of the light source. This way, we could ensure that the variations are solely due to changes of the PMF temperature. We found the setup to be invariant to changes with respect to time.

In a next step, the axial resolution of both channels were measured - the undelayed channel (channel 1) and delayed channel (channel 2) - at temperatures ranging from 12.5 °C to 42.5 °C. The normalized intensity was plotted logarithmically for both cases. The results can be seen in Fig.2.
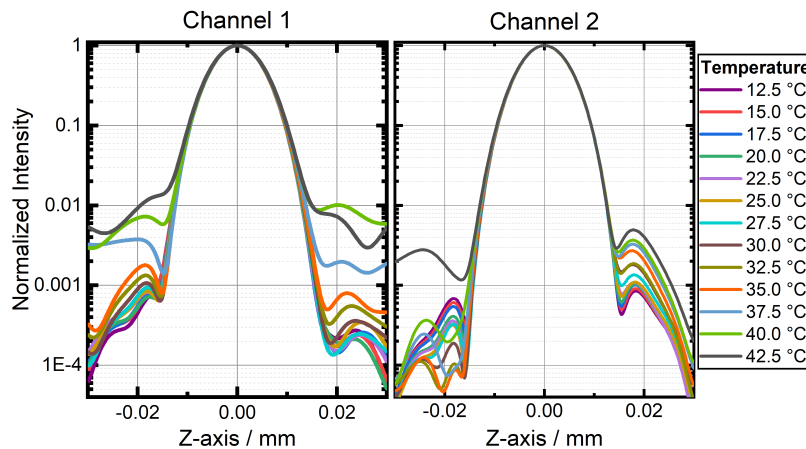

Fig. 2. Logarithmic representation of the axial resolution in both channels to illustrate the variation of axial resolution with ambient temperatures of solely the PMF.

From these graphs, we can deduce the overall picture that the pedestals of the peaks are rising with increasing temperature. Furthermore, the effect varies from channel 1 to channel 2. To further analyze this behavior, the FWHM of each peak was evaluated and plotted as a function of temperature. The result can be seen in Fig.3.
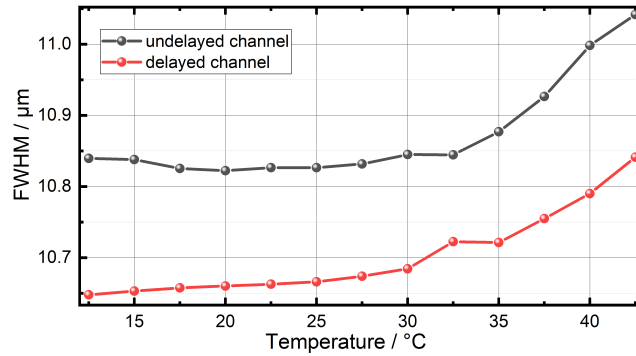
Fig. 3. Evaluated FWHM as a function of temperature for the delayed and undelayed channel.

An increased amount of unbalanced dispersion to the setup with increasing temperature leads to a broadening of about 0.2 μm in the FWHM of both channels when varying the temperature by 30 °C. Using CMSI, the dispersion of the system was measured for varying temperatures. We found that the PMD is decreasing at higher temperatures, illustrated by the red curve in Fig.4. While varying the temperature, we encountered an additional implication. When the PMF is heated up, its effective length increases. This dependence changes the "g" and "h" functions of the system such that the peaks, to which the formalism initially was applied to, will not only deviate from their initial shape, but also from their axial position. Consequently, not only changes in the group velocity dispersion of the fiber occur, but also drifts in the OPD as well as the separation between the 2 channels need to be considered with temperature variation. In the resulting A-scan image, this will appear as a drift of one of the multiplexed images. The magnitude of the drift and the corresponding peak position of both channels were investigated and are plotted with respect to temperature change in Fig.4.
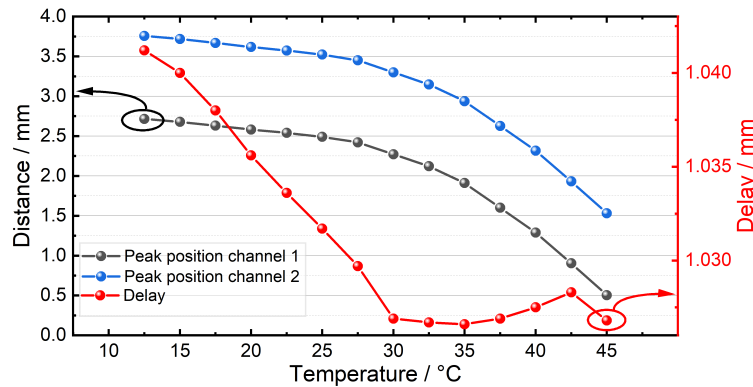

Fig. 4. Axial drift with respect to temperature. The delay between the channels is plotted on the right y-axis.

As shown in Fig.4, the variation in the peak positions leads to a drift of more than 2 mm by a temperature change of 30 °C. This drift is relatively large and can cause the A-scan signals of each

corresponding channel to deviate significantly from the accurate "g" and "h" coverage obtained in the master stage in the CMSI algorithm, leading to a highly distorted or not appropriate OCT image. The delay between the channels varies with temperature. Due to the PMD, the ratio of drift to temperature change also varies nonlinearly. In practice, precise knowledge of the OPD, the variation in delay dispersion with temperature change in PMF and accurate temperature control are required when using a fiber based PS-OCT system over a long period of time.

To see the impact of temperature variation in an OCT image with depth-resolved DPPR and orientation distributions, a plastic hair comb with birefringence characteristics was investigated as shown in Fig.5.
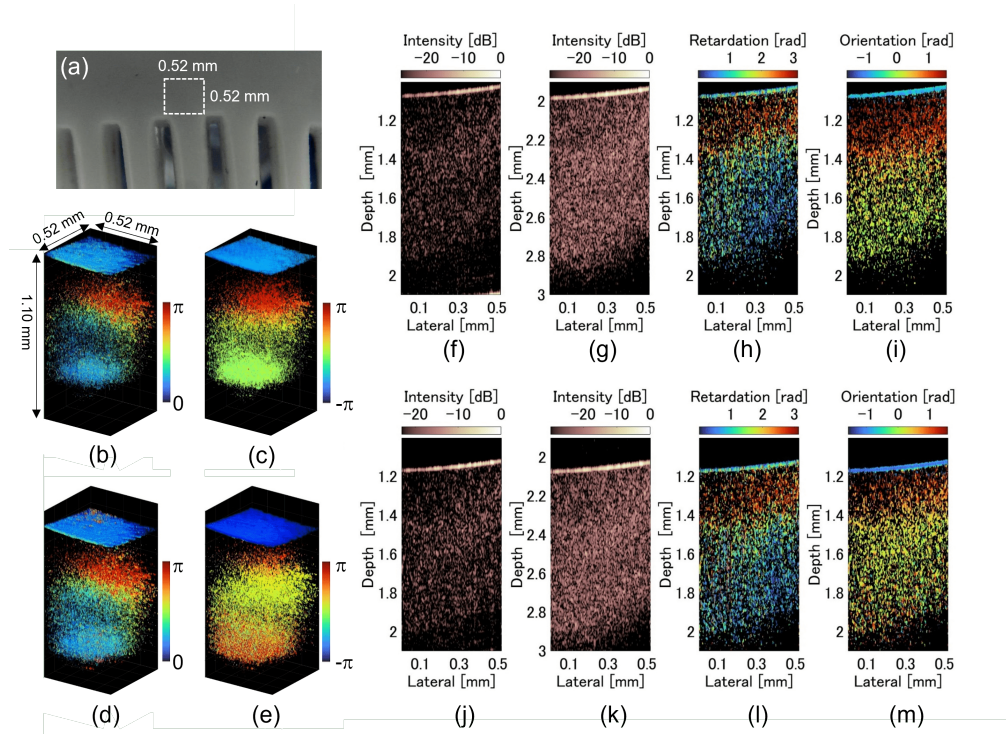

Fig. 5. Retardation and orientation distributions of a plastic hair comb. (a) photograph of the sample and measurement area (dotted line), (b) and (c) 3D distributions of the DPPR and orientation of the plastic hair comb at a PMF temperature of 20 °C. (d) and (e) same distributions at a PMF temperature of 25 °C. (f), (g), (h) and (i) non-delayed OCT image (channel 1) obtained by $|PM1\text{-}H|^2 + |PM1\text{-}V|^2$, delayed OCT-image (channel 2) obtained by $|PM2\text{-}H|^2 + |PM1\text{-}V|^2$, DPPR distribution and orientation distribution, respectively at a PMF temperature of 20 °C, (j), (k), (l) and (m) same tomographic distributions at a temperature of 25 °C.

B-scans were performed while locking the temperature of the PMF at 20°C and 25°C, respectively. This margin corresponds to possible fluctuations in ambient room temperature. The measurements were performed in the region marked in Fig.5 (a), the area where the comb teeth begin to elongate due to the extrusion of the polymer in the manufacturing process. Fig.5 (b), (c) and (f)-(i) show the OCT images and birefringence analysis results at 20 °C. For an accurate comparison, the identical series of measurements are provided for a temperature of 25 °C in Fig.5 (d), (e) and (j)-(m). The results were obtained by detecting changes due to drift and correcting the surface position to calculate the polarization. The observed signal drifted

for variations in temperature and was within the range predicted in Fig.4. The observed drift was not large enough to cause major degradation in CMSI applications. However, even small changes may have a significant impact on the calculation of birefringence in our PS-OCT and can lead to different results. This is because the detection of the sample surface is essential for determining polarization DPPR and orientation [40]. If the shift is not taken into account, appropriate polarization distribution would not be obtained by fallacies in the surface detection. Therefore, the detection of the surface position needed to be corrected with regards to temperature changes. The phase distributions of the OCT signals were obtained by applying the k-clock provided by the SS and the CMSI method. The DPPR distributions are displayed in Fig.5 (b), (d), (h) and (l), indicating experimentally that this system can measure retardation and orientation distribution properly with accurate PMF temperature control and compensation of the drift.

The orientation can be seen in Fig.5 (c), (e), (i) and (m). Here, it was observed that the entire slopes and values varied more significantly with temperature variation than the DPPR distributions, as indicated in Fig. 6.
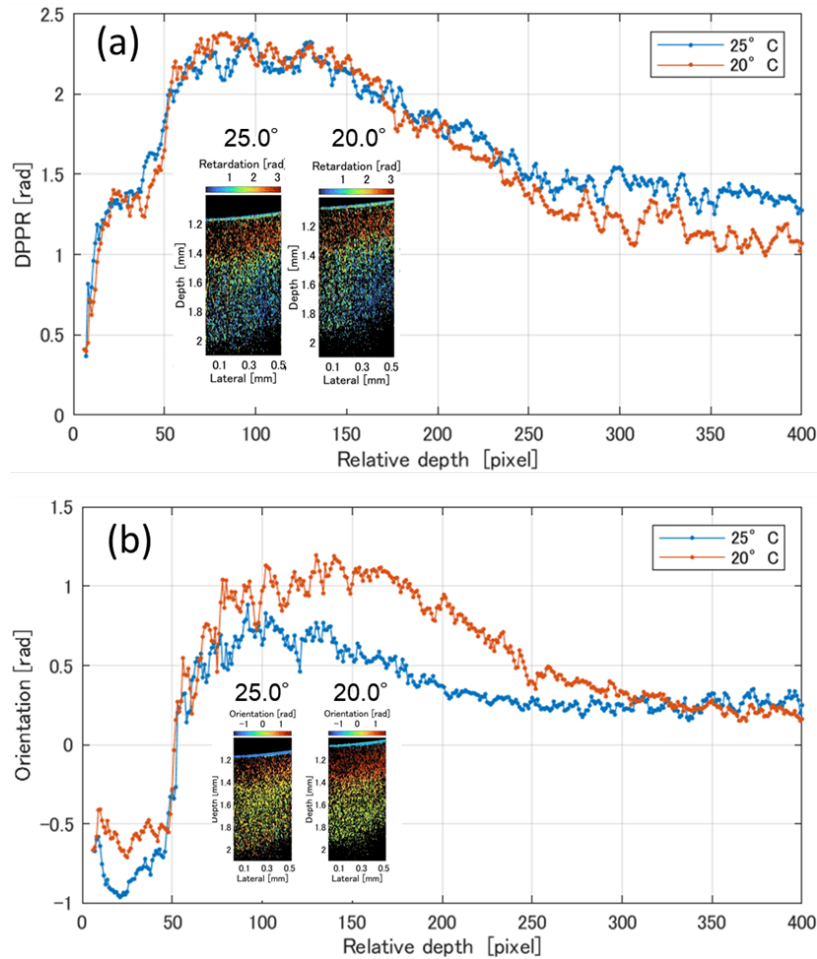

Fig. 6. Average distribution slopes along the depth direction of the DPPR at 20°C and 25°C and (b) averaging orientation slopes at 20°C and 25°C.

One possible explanation for this difference could be that the DPPR of the polarization multiplexing method removes the effect of birefringence in the optical fiber from the sample

surface to the detectors, whereas the orientation was calculated directly as a cumulative azimuthal angle of elliptical polarization from the observed Jones matrix, which is considered to be more sensitive to changes in the surroundings of the fiber system caused by temperature variation. In a next step, the impact of ambient temperature fluctuations of the PMF were investigated when imaging a biological sample. In this experiment, raw chicken sternum cartilage containing water and collagen was used as a sample. Fig.7 displays three-dimensional tomographic retardation and orientation distributions of cartilage. For the DPPR distribution, the overall trend appeared to be similar, although small local errors could be observed in the measurement.
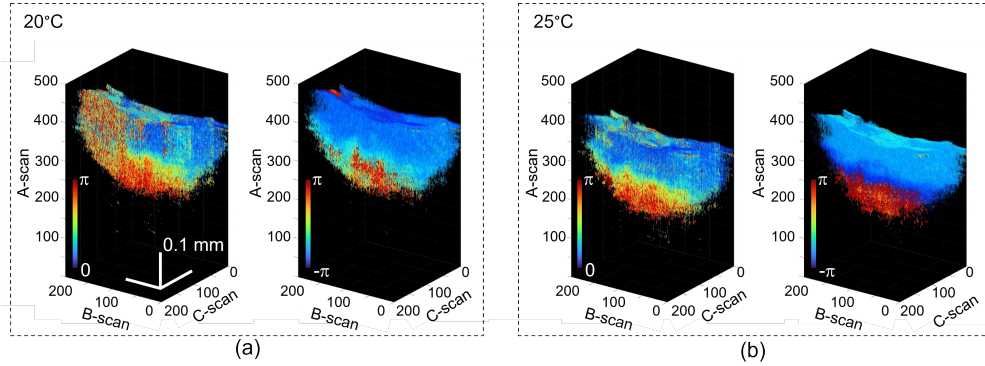

Fig. 7. Volumetric retardation and orientation distributions of chicken sternum cartilage distributions of chicken sternum cartilage, (a) DPPR (left) and orientation (right) with the PMF set at 20 °C, (b) same distributions set at 25 °C. The size of the volume was 0.52 mm(W) x 0.52 mm(D) x 1.1 mm(H), corresponding to the resolution of 200(W)x200(D)x500(H) voxel. In the data displayed, an OCT signal strength of -35 dB or less with respect to the maximum intensity was omitted from the calculations.

Differences originating from the variations in temperature changes and systematic errors due to repeated measurements of wet and soft biological samples over a long period of time need to be carefully distinguished at this point. In addition to comparing overall trends, cross-sectional images of B-scans and C-scans are shown in Fig.8.
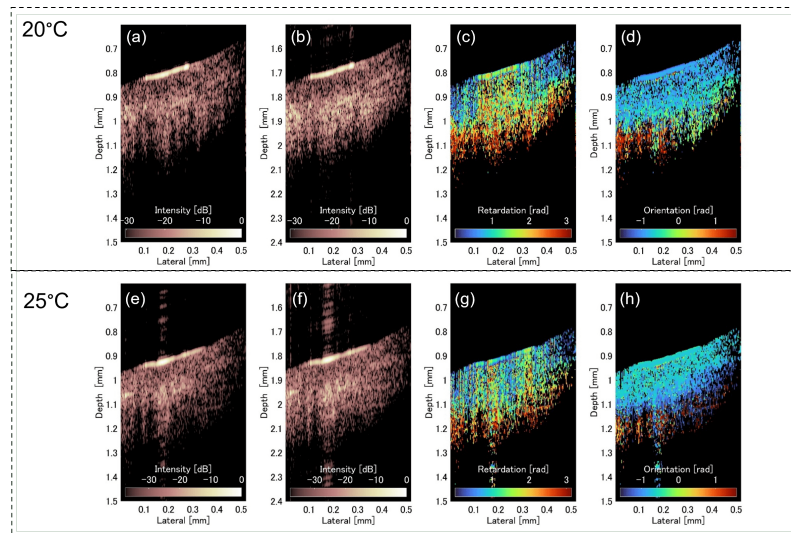
Fig. 8. B-scan images at the 100th pixel position of the volumetric C-scan distributions from Fig.7. (a), (e) non-delayed OCT image; (b), (f) delayed OCT image; (c), (g) DPPR and (d), (h) orientation of the biological sample. The measurements were performed at a PMF temperature of 25 °C and 20 °C, respectively.

In the presented B- and C-scans, the DPPR distribution appeared to have a tendency to increase the phase delay along the depth direction at both temperatures. To guarantee stable temperature operation, the measurements were taken about 10 minutes apart from each other. This, however, can lead to slight misalignments of the biological sample containing moisture. Furthermore, the shift of the lens focus position was caused by the drift of the OPD. As a consequence, the precise detection of the surface position for the DPPR calculation can be compromised. When taking these uncertainties into account, there is little difference in the DPPR distribution. The results were reproducible among multiple sets of consecutive measurements. On the other hand, it could be confirmed that the gradient of orientation was reversed by temperature change, as indicated in Fig.8 (d), (h). This shows a definite difference when compared to the variation in DPPR. The fluctuation in orientation values need to be considered in the same manner as elaborated in the results of the plastic hair comb measurements in Fig.5. Therefore, the external factors and systematic errors altering the polarization state, such as fiber temperature and physical distortions, need to be carefully taken into account before visualizing the orientation.

4.   Conclusion

We report on the first characterization of temperature effects in a PS-OCT system that uses a PMF as a passive delay unit. The resulting degradation of imaging performance in all-fiber based PS-OCT setups is demonstrated. Variations in the temperature lead to a change in effective fiber length of the PMF which causes a drift in the system and changes the OPD. In addition to that, it was demonstrated that the polarization mode dispersion decreases with increasing temperature, which leads to a broadening in the detection of both delayed and undelayed channel accuracy. Using a temperature controller, as well as the k-clock provided by the light source, we successfully stabilised variations arising from changes in temperature and characterized them. The reported behavior seems to be stable with regards to changes over time. For imaging the retardation and orientation, we first investigated a plastic hair comb displaying birefringent features while varying the PMF temperature. Apart from the described shift, no significant changes could be identified in neither the DPPR, nor the orientation of the sample. Next, a biological sample

was investigated in the same manner as the plastic hair comb. While no changes in the DPPR could be identified, the orientation did vary with temperature change. We believe the cause of the latter could be due to temporal changes in the sample under investigation, however further measurements are required to fully confirm this cause. We hope that these findings can be highly beneficial for future depth-encoded, fiber-based PS-OCT setups as this approach represents a simpler, more compact and robust solution than bulk components, making it feasible for potential clinical imaging applications.

5. Backmatter

References

1. D. Huang, E. A. Swanson, C. P. Lin, J. S. Schuman, W. G. Stinson, W. Chang, M. R. Hee, T. Flotte, K. Gregory, C. A. Puliafito, and J. G. Fujimoto, "Optical Coherence Tomography," Science **254**, 1178–1181 (1991).
2. N. M. Israelsen, M. Maria, M. Mogensen, S. Bojesen, M. Jensen, M. Haedersdal, A. Podoleanu, and O. Bang, "The value of ultrahigh resolution oct in dermatology - delineating the dermo-epidermal junction, capillaries in the dermal papillae and vellus hairs," Biomed. Opt. Express **9**, 2240–2265 (2018).
3. M. R. Hee, E. A. Swanson, J. G. Fujimoto, and D. Huang, "Polarization-sensitive low-coherence reflectometer for birefringence characterization and ranging," J. Opt. Soc. Am. B **9**, 903 (1992-06-01).
4. J. P. McLean, Y. Gan, T. H. Lye, D. Qu, H. H. Lu, and C. P. Hendon, "High-speed collagen fiber modeling and orientation quantification for optical coherence tomography imaging," Opt. Express **27**, 14457 (2019-05-13).
5. W. Li, B. F. Narice, D. O. Anumba, and S. J. Matcher, "Polarization-sensitive optical coherence tomography with a conical beam scan for the investigation of birefringence and collagen alignment in the human cervix," Biomed. Opt. Express **10**, 4190 (2019-08-01).
6. M. Pircher, C. K. Hitzenberger, and U. Schmidt-Erfurth, "Polarization sensitive optical coherence tomography in the human eye," Prog. Retin. Eye Res. **30**, 431–451 (2011-11).
7. C. K. Hitzenberger, E. Götzinger, M. Sticker, M. Pircher, and A. F. Fercher, "Measurement and imaging of birefringence and optic axis orientation by phase resolved polarization sensitive optical coherence tomography," Opt. Express **9**, 780–790 (2001).
8. M. Pircher, E. Goetzinger, R. Leitgeb, and C. K. Hitzenberger, "Transversal phase resolved polarization sensitive optical coherence tomography," Phys. Med. Biol. **49**, 1257–1263 (2004-04-07).
9. R. G. Cucu, J. Pedro, R. B. Rosen, and A. G. Podoleanu, "Polarization-sensitive OCT system using single-mode fiber," in *Photonics North 2004: Photonic Applications in Telecommunications, Sensors, Software, and Lasers,* J. C. Armitage, R. A. Lessard, and G. A. Lampropoulos, eds. (2004-11-16), p. 170.
10. Y. Lim, M. Yamanari, S. Fukuda, Y. Kaji, T. Kiuchi, M. Miura, T. Oshika, and Y. Yasuno, "Birefringence measurement of cornea and anterior segment by office-based polarization-sensitive optical coherence tomography," Biomed. Opt. Express **2**, 2392 (2011-08-01).
11. B. Cense, T. C. Chen, B. H. Park, M. C. Pierce, and J. F. De Boer, "In vivo depth-resolved birefringence measurements of the human retinal nerve fiber layer by polarization-sensitive optical coherence tomography," Opt. Lett. **27**, 1610 (2002-09-15).
12. M. Pircher, E. Götzinger, R. Leitgeb, H. Sattmann, O. Findl, and C. K. Hitzenberger, "Imaging of polarization properties of human retina in vivo with phase resolved transversal PS-OCT," Opt. Express **12**, 5940 (2004-11-29).
13. A. G. Podoleanu, R. G. Cucu, and R. B. Rosen, "In vivo t-scan-based polarization-sensitive OCT of the optic nerve," in *Coherence Domain Optical Methods and Optical Coherence Tomography in Biomedicine VIII,* V. V. Tuchin, J. A. Izatt, and J. G. Fujimoto, eds. (2004-07-01), p. 300.
14. M. Pircher, E. Go¨tzinger, O. Findl, S. Michels, W. Geitzenauer, C. Leydolt, U. Schmidt-Erfurth, and C. K. Hitzenberger, "Human macula investigated in vivo with polarization-sensitive optical coherence tomography," Investig. Opthalmology & Vis. Sci. **47**, 5487 (2006-12-01).
15. J. Strasswimmer, M. C. Pierce, B. H. Park, V. Neel, and J. F. De Boer, "Polarization-sensitive optical coherence tomography of invasive basal cell carcinoma," J. Biomed. Opt. **9**, 292 (2004).
16. M. Pircher, E. Goetzinger, R. Leitgeb, and C. K. Hitzenberger, "Three dimensional polarization sensitive OCT of human skin in vivo," Opt. Express **12**, 3236 (2004-07-12).

17. M. C. Pierce, J. Strasswimmer, B. Hyle Park, B. Cense, and J. F. De Boer, "Birefringence measurements in human skin using polarization-sensitive optical coherence tomography," J. Biomed. Opt. **9**, 287 (2004).

18. Y. Yasuno, S. Makita, Y. Sutoh, M. Itoh, and T. Yatagai, "Birefringence imaging of human skin by polarization-sensitive spectral interferometric optical coherence tomography," Opt. Lett. **27**, 1803 (2002-10-15).

19. X.-J. Wang, T. E. Milner, J. F. De Boer, Y. Zhang, D. H. Pashley, and J. S. Nelson, "Characterization of dentin and enamel by use of optical coherence tomography," Appl. Opt. **38**, 2092 (1999-04-01).

20. A. Baumgartner, S. Dichtl, C. Hitzenberger, H. Sattmann, B. Robl, A. Moritz, A. Fercher, and W. Sperr, "Polariza-tion–sensitive optical coherence tomography of dental structures," Caries Res. **34**, 59–69 (2000).

21. S. K. Nadkarni, M. C. Pierce, B. H. Park, J. F. De Boer, P. Whittaker, B. E. Bouma, J. E. Bressner, E. Halpern, S. L. Houser, and G. J. Tearney, "Measurement of collagen and smooth muscle cell content in atherosclerotic plaques using polarization-sensitive optical coherence tomography," J. Am. Coll. Cardiol. **49**, 1474–1481 (2007-04).

22. W.-C. Kuo, N.-K. Chou, C. Chou, C.-M. Lai, H.-J. Huang, S.-S. Wang, and J.-J. Shyu, "Polarization-sensitive optical coherence tomography for imaging human atherosclerosis," Appl. Opt. **46**, 2520 (2007-05-01).

23. S. D. Giattina, B. K. Courtney, P. R. Herz, M. Harman, S. Shortkroff, D. L. Stamper, B. Liu, J. G. Fujimoto, and M. E. Brezinski, "Assessment of coronary plaque collagen with polarization sensitive optical coherence tomography (PS-OCT)," Int. J. Cardiol. **107**, 400–409 (2006-03).

24. A. L. James, T. R. Bai, T. Mauad, M. J. Abramson, M. Dolhnikoff, K. O. McKay, P. S. Maxwell, J. G. Elliot, and F. H. Green, "Airway smooth muscle thickness in asthma is related to severity but not duration of asthma," Eur. Respir. J. **34**, 1040–1045 (2009-11-01).

25. A. L. James and S. Wenzel, "Clinical relevance of airway remodelling in airway diseases," Eur. Respir. J. **30**, 134–155 (2007-03-14).

26. D. C. Adams, L. P. Hariri, A. J. Miller, Y. Wang, J. L. Cho, M. Villiger, J. A. Holz, M. V. Szabari, D. L. Hamilos, R. Scott Harris, J. W. Griffith, B. E. Bouma, A. D. Luster, B. D. Medoff, and M. J. Suter, "Birefringence microscopy platform for assessing airway smooth muscle structure and function in vivo," Sci. Transl. Med. **8** (2016-10-05).

27. M. Castro, A. S. Rubin, M. Laviolette, J. Fiterman, M. De Andrade Lima, P. L. Shah, E. Fiss, R. Olivenstein, N. C. Thomson, R. M. Niven, I. D. Pavord, M. Simoff, D. R. Duhamel, C. McEvoy, R. Barbers, N. H. Ten Hacken, M. E. Wechsler, M. Holmes, M. J. Phillips, S. Erzurum, W. Lunn, E. Israel, N. Jarjour, M. Kraft, N. S. Shargill, J. Quiring, S. M. Berry, and G. Cox, "Effectiveness and safety of bronchial thermoplasty in the treatment of severe asthma: A multicenter, randomized, double-blind, sham-controlled clinical trial," Am. J. Respir. Crit. Care Med. **181**, 116–124 (2010-01-15).

28. F. Feroldi, J. Willemse, V. Davidoiu, M. G. O. Gräfe, D. J. Van Iperen, A. W. M. Goorsenberg, J. T. Annema, J. M. A. Daniels, P. I. Bonta, and J. F. De Boer, "In vivo multifunctional optical coherence tomography at the periphery of the lungs," Biomed. Opt. Express **10**, 3070 (2019-06-01).

29. M. Vaselli, P. C. Wijsman, J. Willemse, A. W. Goorsenberg, F. Feroldi, J. N. d'Hooghe, J. T. Annema, J. F. De Boer, and P. I. Bonta, "Polarization sensitive optical coherence tomography for bronchoscopic airway smooth muscle detection in bronchial thermoplasty-treated patients with asthma," Chest **160**, 432–435 (2021-08).

30. M. Villiger, D. Lorenser, R. A. McLaughlin, B. C. Quirk, R. W. Kirk, B. E. Bouma, and D. D. Sampson, "Deep tissue volume imaging of birefringence through fibre-optic needle probes for the delineation of breast tumour," Sci. Reports **6**, 28771 (2016-07-01).

31. J. Willemse, M. G. Gräfe, F. D. Verbraak, and J. F. De Boer, "In vivo 3d determination of peripapillary scleral and retinal layer architecture using polarization-sensitive optical coherence tomography," Transl. Vis. Sci. & Technol. **9**, 21 (2020-10-19).

32. J.-g. Zheng, T. Huo, N. Tian, T. Chen, C. Wang, N. Zhang, F. Zhao, D. Lu, D. Chen, W. Ma, J.-l. Sun, and P. Xue, "Noninvasive three-dimensional live imaging methodology for the spindles at meiosis and mitosis," J. Biomed. Opt. **18**, 050505 (2013-05-09).

33. J.-g. Zheng, T. Huo, T. Chen, C. Wang, N. Zhang, N. Tian, F. Zhao, D. Lu, D. Chen, W. Ma, J.-l. Sun, and P. Xue, "Understanding three-dimensional spatial relationship between the mouse second polar body and first cleavage plane with full-field optical coherence tomography," J. Biomed. Opt. **18**, 010503 (2012-12-13).

34. J.-g. Zheng, T. Chen, C. Wang, N. Tian, F. Zhao, T. Huo, N. Zhang, D. Chen, W. Ma, J.-L. Sun, P. Xue, and D. Lu, "Label-free subcellular 3d live imaging of preimplantation mouse embryos with full-field optical coherence tomography," J. Biomed. Opt. **17**, 1 (2012-06-28).

35. W.-H. Wang, L. Meng, R. J. Hackett, R. Odenbourg, and D. L. Keefe, "Limited recovery of meiotic spindles in living human oocytes after cooling–rewarming observed using polarized light microscopy," Hum. Reproduction **16**, 2374–2378 (2001-11).

36. L. Liu, J. R. Trimarchi, R. Oldenbourg, and D. L. Keefe, "Increased birefringence in the meiotic spindle provides a new marker for the onset of activation in living oocytes1," Biol. Reproduction **63**, 251–258 (2000-07-01).

37. M. J. Marques, S. Rivet, A. Bradu, and A. Podoleanu, "Polarization-sensitive optical coherence tomography system tolerant to fiber disturbances using a line camera," Opt. Lett. **40**, 3858 (2015).

38. E. Götzinger, B. Baumann, M. Pircher, and C. K. Hitzenberger, "Polarization maintaining fiber based ultra-high resolution spectral domain polarization sensitive optical coherence tomography," Opt. Express **17**, 22704–22717 (2009).

39. B. Baumann, W. Choi, B. Potsaid, D. Huang, J. S. Duker, and J. G. Fujimoto, "Swept source / fourier domain polarization sensitive optical coherence tomography with a passive polarization delay unit," Opt. Express **20**,

10229–10241 (2012).

40. Z. Wang, H.-C. Lee, O. O. Ahsen, B. Lee, W. Choi, B. Potsaid, J. Liu, V. Jayaraman, A. Cable, M. F. Kraus, K. Liang, J. Hornegger, and J. G. Fujimoto, "Depth-encoded all-fiber swept source polarization sensitive OCT," Biomed. Opt. Express **5**, 2931 (2014-09-01).

41. A. Bradu, N. M. Israelsen, M. Maria, M. J. Marques, S. Rivet, T. Feuchter, O. Bang, and A. Podoleanu, "Recovering distance information in spectral domain interferometry," Sci. Reports **8**, 15445 (2018-10-18). Number: 1 Publisher: Nature Publishing Group.

42. S. Rivet, M. Maria, A. Bradu, T. Feuchter, L. Leick, and A. Podoleanu, "Complex master slave interferometry," Opt. Express **24**, 2885 (2016-02-08). Number: 3.

43. A. Bradu, K. Kapinchev, F. Barnes, and A. Podoleanu, "Master slave en-face oct/slo," Biomed. Opt. Express **6**, 3655 (2015-09-01). Number: 9.

44. C. Chin, A. Bradu, R. Lim, M. Khandwala, J. Schofield, L. Leick, and A. Podoleanu, "Master/slave optical coherence tomography imaging of eyelid basal cell carcinoma," Appl. Opt. **55**, 7378 (2016-09-10). Number: 26.

45. A. Bradu, S. Rivet, and A. Podoleanu, "Master/slave interferometry – ideal tool for coherence revival swept source optical coherence tomography," Biomed. Opt. Express **7**, 2453 (2016-07-01). Number: 7.

46. B. H. Park, M. C. Pierce, B. Cense, and J. F. de Boer, "Jones matrix analysis for a polarization-sensitive optical coherence tomography system using fiber-optic components," Opt. Lett. **29**, 2512–2514 (2004).

47. S. Makita, M. Yamanari, and Y. Yasuno, "Generalized jones matrix optical coherence tomography: performance and local birefringence imaging," Opt. Express **18**, 854–876 (2010).

48. S. Rivet, M. J. Marques, A. Bradu, and A. Podoleanu, "Optical module to extend any fourier-domain optical coherence tomography system into a polarisation-sensitive system," J. Opt. **18**, 065607 (2016).